Advances in Nano Research, *Vol. 19, No. 1 (2025) 41-51*
https://doi.org/10.12989/anr.2025.19.1.041

An n-order refined plate theory for bending and buckling of functionally graded polymer composite plates reinforced with graphene nanoplatelets

Vagelis Plevris*[1], Lazreg Hadji[2a] and Hassen Ait Atmane[3b]

[1]*Department of Civil and Environmental Engineering, College of Engineering, Qatar University, P.O. Box: 2713, Doha, Qatar*
[2]*Department of Civil Engineering, University of Tiaret, BP 78 Zaaroura, Tiaret,14000, Algeria*
[3]*Civil Engineering Department, University of Hassiba Ben Bouali, Chlef 02180, Algeria*

(*Received January 2, 2025, Revised April 15, 2025, Accepted July 1, 2025*)

Abstract. This study investigates the bending and buckling behavior of functionally graded multilayer graphene nanoplatelet (GPL)/polymer composite plates using an n-order refined plate theory. The theory introduces a higher-order polynomial displacement field that ensures variational consistency and eliminates the need for shear correction factors. In this formulation, shear stresses vary parabolically through the plate thickness, and stress-free conditions are satisfied at both the top and bottom surfaces, resulting in improved accuracy compared to conventional plate theories. A key innovation of this work lies in the layer-wise variation of GPL weight fractions, enabling the design of functionally graded nanocomposites with both uniform and non-uniform reinforcement patterns—specifically, UD, FG-O, FG-X, and FG-A. While most existing studies are limited to uniformly distributed GPLs or rely on lower-order theories, this study addresses these limitations by proposing an analytically tractable higher-order model that can accurately capture shear deformation effects and by systematically analyzing the mechanical influence of different GPL distribution patterns. This dual advancement fills an important gap in the literature, particularly in understanding the performance of non-uniformly graded nanocomposites under bending and buckling. The effective Young's modulus is predicted using the Halpin-Tsai micromechanics model, and the rule of mixtures is used to determine the effective Poisson's ratio and mass density. Analytical solutions for static deflection and buckling are derived for simply supported plates using the Navier solution technique. The results show that non-uniform GPL distributions, particularly FG-X and FG-O, significantly enhance bending stiffness and buckling resistance by concentrating reinforcement near high-stress regions. Additionally, increasing the GPL weight fraction and optimizing GPL geometry further improve structural performance. This study offers new insights into the tailored design of functionally graded nanocomposite plates and provides practical guidance for lightweight, high-performance structural components in aerospace, automotive, and civil engineering applications.

Keywords: functionally graded nanocomposites; Graphene nanoplatelets (GPLs); nanocomposite plates; n-order four variable refined theory; polymer composites

1. Introduction

Polymer composites filled with carbon-based materials have revolutionized engineering applications due to their outstanding mechanical, thermal, and electrical properties. These materials are particularly significant in fields such as aerospace, automotive, biomedical, and civil engineering, where performance and weight efficiency are critical design considerations (Bellucci *et al*. 2007). Among carbon-based reinforcements, graphene nanoplatelets (GPLs) have emerged as a superior choice, offering high mechanical strength, large specific surface areas, and cost-effective production (Huang *et al*. 2012). Even at low weight fractions, GPLs impart remarkable improvements in the mechanical (Montazeri and Rafii-Tabar 2011, Potts *et al*. 2011, Rafiee *et al*. 2010, Rafiee *et al*. 2009a, b), thermal (Mortazavi *et al*. 2013, Wang *et al*. 2015), and electrical properties (Wang *et al*. 2015) of polymer matrices. These advancements make GPL-reinforced polymer nanocomposites highly attractive for developing lightweight, high-performance structural materials.

In addition, recent advancements in the analysis of functionally graded materials (FGMs) and nanoplates have highlighted the importance of incorporating nonlocal elasticity, surface effects, and advanced numerical techniques. Several studies have focused on the buckling behavior of FGMs, showing how nonlocal and surface effects significantly influence structural stability (Ansari and Norouzzadeh 2016, Norouzzadeh and Ansari 2018). Using isogeometric and finite element methods, researchers have provided robust frameworks for analyzing both static and dynamic responses of FG nanoplates (Ansari *et al*. 2018, Norouzzadeh *et al*. 2018). The Asymptotic Numerical Method, in particular, has been effectively used for the buckling and post-buckling analysis of FGM plates (Sitli *et al*. 2021), while other studies have explored thermal and porosity-dependent effects in such materials (Joueid *et al*. 2024). A dynamic approach has also been proposed for buckling analysis, emphasizing the influence of time-

*Corresponding author, Associate Professor,
E-mail: vplevris@qu.edu.qa
[a] Professor, E-mail: lazreg.hadji@univ-tiaret.dz
[b] Professor, E-mail: aitatmane2000@yahoo.fr

ISSN: 2287-237X (Print), 2287-2388 (Online)

dependent loading conditions (Swaminathan *et al*. 2021). Moreover, the nonlinear behavior of micropolar plates has been addressed using nonclassical finite element methods (Ansari *et al*. 2017). Complementary to these efforts, Moita *et al*. (2020) investigated the buckling response of composite and FGM plates, providing further validation for theoretical models. These contributions collectively advance the modeling accuracy and predictive capabilities in the structural analysis of FGMs.

The design and analysis of functionally graded GPL/ polymer nanocomposites present significant challenges due to their non-uniform material distribution. These composites exhibit spatially varying properties across their thickness, influenced by the specific arrangement of GPLs. Conventional plate theories often rely on simplifying assumptions or empirical corrections, which may compromise accuracy in capturing the mechanical behavior of these advanced materials. Recent studies have highlighted the complexities involved in modeling such non-uniform distributions. For instance, Ebrahimi *et al*. (2024) examined wave propagation in thermally loaded GPL-reinforced nanocomposite plates, emphasizing the need for refined analytical approaches to accurately predict their behavior. Similarly, Cong and Duc (2018) developed an analytical method to investigate the nonlinear dynamic response of functionally graded multilayer nanocomposite plates reinforced with GPLs, underscoring the limitations of traditional theories in addressing the unique characteristics of these materials. Therefore, there is a pressing need for advanced analytical methods that can effectively address these complexities and facilitate the optimal design of functionally graded GPL/polymer nanocomposites.

Daikh *et al*. (2023) conducted an analytical investigation into the static behavior of functionally graded graphene-reinforced composite (FG-GRC) coated plates and shells. Using a complex power-law function to describe material gradation, they explored hardcore and softcore configurations under various boundary conditions. The equilibrium equations were derived using the virtual work approach and solved with the Galerkin technique, with results validated against reliable published studies. Drai *et al*. (2023) developed a modified analytical model to analyze the bending behavior of axially functionally graded carbon nanotubes reinforced composite nanobeams. Using higher-order shear deformation theory and a modified nonlocal strain gradient theory, the study accounted for nanoscale effects and parabolic shear variations. The mechanical properties were derived through an extended rule of mixtures and molecular dynamics simulations, with carbon nanotubes distributed axially via a two-parameter power grading function. Solving the equilibrium equations with Navier's procedure, the model evaluated the impact of inhomogeneity, geometry, and nanoscale parameters on deflections and stresses, offering a valuable framework for designing micro- and nanoelectromechanical (MEMS and NEMS) systems.

In this context, the present work employs an *n*-order refined plate theory for investigating the static bending and buckling behaviors of functionally graded GPL/polymer nanocomposite plates. The *n*-order shear deformation theory, (Xiang *et al*. 2011) provides a flexible framework for accurately modeling shear deformation effects without requiring shear correction factors. In the current study, this theory is extended and applied to the analysis of multilayer plates with non-uniform GPL distributions. The displacement field incorporates higher-order polynomial terms, ensuring variational consistency and capturing the parabolic distribution of transverse shear stresses, which vanish at the plate surfaces—thereby improving the accuracy of mechanical response predictions.

The study utilizes the modified Halpin-Tsai model (Song *et al*. 2017) to estimate the effective Young's modulus and the rule of mixtures to determine the Poisson's ratio and mass density. These models were chosen due to their proven effectiveness in modeling nanocomposites reinforced with high-aspect-ratio fillers such as graphene nanoplatelets. The Halpin-Tsai model captures the influence of filler geometry and orientation on the mechanical stiffness, while the rule of mixtures provides a straightforward yet effective approach to account for the spatial variation of material properties across the plate thickness. Together, these models offer a good balance between accuracy and analytical tractability, making them particularly suitable for parametric studies and closed-form solutions. Analytical solutions are derived for simply supported plates under static and buckling loads using the Navier solution technique. The effects of GPL weight fraction, distribution patterns, and geometry on the plates' mechanical performance are systematically evaluated, providing new insights into the optimization of these materials.

Unlike existing studies that often focus on uniformly distributed reinforcements, this work explores both uniform and non-uniform GPL distribution patterns, including Uniform Distribution (UD), Functionally Graded with maximum concentration at the mid-plane (FG-O), Functionally Graded with maximum concentration at the outer surfaces (FG-X), and an Asymmetric Graded pattern (FG-A). Such distributions allow for tailored mechanical properties by strategically placing GPLs in regions of high stress.

The outcomes of this research have significant implications for the design of next-generation functionally graded nanocomposite plates. Potential applications span diverse industries such as aerospace, automotive, and civil engineering, where lightweight and durable materials are critical. This work also lays the foundation for further exploration of advanced nanocomposite designs, including the incorporation of hybrid reinforcements and their performance under dynamic and thermal loads.

The structure of the paper is as follows: Section 1 is the introduction, outlining the motivation, objectives, and scope of the study. Section 2 presents the formulation of the problem, detailing the governing equations, material properties, and the key assumptions of the proposed *n*-order refined plate theory. Section 3 describes the analytical solution methodology, employing the Navier solution technique to derive expressions for bending and buckling responses under different conditions. Section 4 discusses numerical results and parametric studies, analyzing the

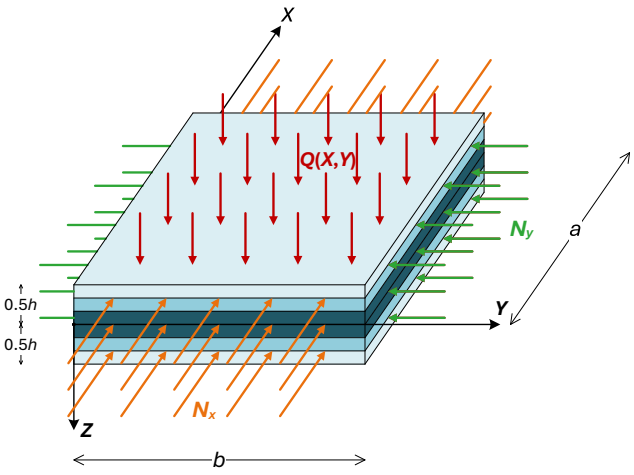

Fig. 1 Laminated graphene platelet (GPL)/polymer composite plate

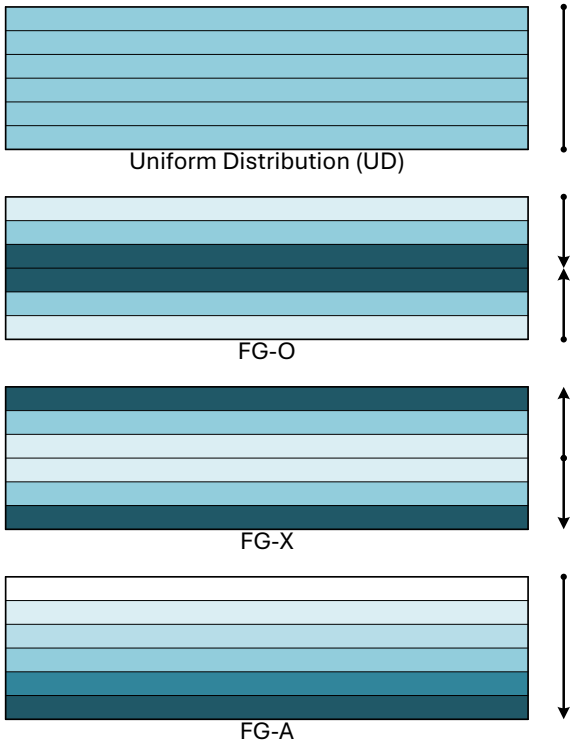

Fig. 2 Four GPL distribution patterns in multilayer GPL/ polymer nanocomposite plates

effects of GPL weight fraction, distribution patterns, and geometry on the mechanical performance of the plates. Finally, Section 5 concludes the work, summarizing the main findings, highlighting their practical relevance, and proposing directions for future research.

2. Problem formulation

Fig. 1 illustrates a multilayered graphene platelet (GPL)/ polymer nanocomposite plate with dimensions defined as length a, width b, and thickness h. The plate is subjected to a transverse static load $q(x, y)$, which acts perpendicular to its surface. The thickness of the plate is divided into N_L uniform layers, each with a thickness of h/N_L. Within each layer, the GPLs are represented as effective rectangular solid fillers that are uniformly dispersed within the polymer matrix. The GPL weight fraction varies across the plate thickness, resulting in a functionally graded structure.

In addition to the transverse load, the plate is subjected to in-plane compressive forces N_x and N_y, acting along the x- and y-directions, respectively. The Cartesian coordinate system originates at the neutral surface of the plate, with the x- and y-axes representing the plate's in-plane dimensions and the z-axis extending through the thickness. The top and bottom surfaces are labeled as $-0.5h$ and $+0.5h$, emphasizing the layered composition and symmetry of the structure.

Fig. 2 illustrates four distinct GPL distribution patterns within the multilayered GPL/polymer nanocomposite plate, each reflecting a unique spatial arrangement of GPL weight fractions across the plate thickness.

• The first configuration, labeled as Uniform Distribution (UD), depicts a constant GPL concentration across all layers, creating an isotropic, homogeneous plate. This distribution assumes identical reinforcement throughout the thickness, serving as a baseline for comparison with non-uniform patterns.

• The second pattern, FG-O, represents a symmetric distribution where the GPL concentration is highest at the mid-plane of the plate and decreases towards the top and bottom surfaces. This arrangement places reinforcement where mid-plane stresses dominate.

• The third configuration, FG-X, also follows a symmetric distribution but contrasts with FG-O by increasing the GPL concentration toward both the top and bottom surfaces. This strategic placement enhances stiffness and resistance to bending by concentrating reinforcement where the maximum stresses occur under loading.

• The fourth pattern, FG-A, is an asymmetric configuration where the GPL weight fraction increases monotonically from the top surface to the bottom surface. Unlike the symmetric patterns, FG-A introduces a gradient that reflects an unequal reinforcement strategy, tailored to specific mechanical performance requirements.

The arrows within Fig. 2 emphasize the direction and intensity of the GPL distribution through the thickness. For FG-O and FG-X, the arrows highlight the symmetry, with FG-O converging towards the mid-plane and FG-X diverging towards the outer surfaces. In FG-A, the arrows indicate a consistent gradient, reinforcing the lack of symmetry in this pattern. Fig. 2 provides a comprehensive visualization of how GPLs can be distributed to tailor the mechanical properties of the nanocomposite plate, allowing engineers to optimize the structure for specific applications by strategically adjusting the GPL arrangements.

2.1 Material properties

The effective Young's modulus of the GPL/polymer nanocomposite, E_C, can be estimated using the Halpin-Tsai micromechanics model (Song *et al.* 2017):

$$E_c^{(k)} = \frac{3}{8}\frac{1+\xi_L\eta_L V_{GPL}}{1-\eta_L V_{GPL}}\cdot E_M + \frac{5}{8}\frac{1+\xi_w\eta_w V_{GPL}}{1-\eta_w V_{GPL}}\cdot E_M \quad (1)$$

The modified Halpin-Tsai model is employed in this study as it offers a robust and physically grounded method for estimating the effective mechanical properties of composites reinforced with high-aspect-ratio nanofillers such as graphene nanoplatelets (GPLs). This model explicitly accounts for key parameters—including the geometry, aspect ratio, and orientation of the GPLs—which critically influence the load-transfer efficiency within the composite. In contrast to more simplified homogenization methods, the Halpin-Tsai model captures the filler–matrix interaction more accurately, leading to reliable predictions of the composite's stiffness. Furthermore, its flexibility in handling spatially varying filler distributions makes it especially suitable for analyzing functionally graded materials, where properties change through the thickness. This capability aligns well with the objectives of the present study, enabling the modeling of complex GPL distributions while preserving analytical tractability and computational efficiency for extensive parametric analyses.

Two additional parameters η_L and η_w are introduced as follows:

$$\eta_L = \frac{(E_{GPL}/E_M) - 1}{(E_{GPL}/E_M) + \xi_L} \tag{2}$$

$$\eta_w = \frac{(E_{GPL}/E_M) - 1}{(E_{GPL}/E_M) + \xi_w} \tag{3}$$

where E_M and E_{GPL} represent the Young's moduli of the polymer matrix and GPLs, respectively, while ξ_L and ξ_w are parameters that depend on the geometry and dimensions of the GPL nanofillers, defined as follows

$$\xi_L = 2(l_{GPL}/h_{GPL}) \tag{4}$$

$$\xi_W = 2(w_{GLP}/h_{GLP}) \tag{5}$$

The parameters l_{GPL}, w_{GPL}, h_{GPL} refer to the average length, width, and thickness of the GPLs, respectively. Furthermore, the volume fraction V_{GPL} in Eq. (1) is defined as follows:

$$V_{GPL} = \frac{g_{GPL}}{g_{GPL} + (\rho_{GPL}/\rho_M) \cdot (1 - g_{GPL})} \tag{6}$$

where g_{GPL} denotes the weight fraction in the nanocomposite, and ρ_M and ρ_{GPL} represent the mass densities of polymer matrix and GPLs, respectively.

The effective Poisson's ratio for the FG composite nanoplate reinforced with GPL is determined using the rule of mixtures and is defined as follows:

$$\nu_c = \nu_{GPL} V_{GPL} + \nu_M V_M \tag{7}$$

where V_M is the volume fraction of the polymer matrix, and ν_M and ν_{GPL} are the Poisson's ratios of the polymer matrix and GPLs, respectively.

2.2 Basic assumptions

The key assumptions of the current theory are as follows:

• The Cartesian coordinate system originates at the neutral surface of the FG plate.

• Displacements are considered small relative to the plate thickness, making the resulting strains infinitesimal.

• The transverse displacement w is composed of two components: bending displacement w_b and shear displacement w_s, both of which are functions of coordinates x and y only:

$$(x, y, z) = w_b(x, y) + w_s(x, y) \tag{8}$$

• The displacements u in the x-direction and v in y-direction are composed of extension, bending, and shear components:

$$u = u_0 + u_b + u_s \tag{9}$$

$$v = v_0 + v_b + v_s \tag{10}$$

• The bending components u_b and v_b are assumed to be consistent with the classical plate theory. Therefore, their expressions are given as:

$$u_b = -z\frac{\partial w_b}{\partial x} \tag{11}$$

$$v_b = -z\frac{\partial w_b}{\partial y} \tag{12}$$

• The shear components u_s and v_s, together with w_s, produce sinusoidal variations in the shear strains γ_{xz} and γ_{yz} and hence to shear stresses τ_{xz} and τ_{yz}, through the plate thickness. These shear stresses are assumed to be zero at the top and bottom surfaces of the plate. Accordingly, the shear components u_s and v_s are expressed as:

$$u_s = -f(z)\frac{\partial w_s}{\partial x} \tag{13}$$

$$v_s = -f(z)\frac{\partial w_s}{\partial y} \tag{14}$$

where

$$f(z) = \frac{z^n}{n}\left(\frac{2}{h}\right)^{n-1} \tag{15}$$

The warping function defined in Eq. (15) is proposed by the authors as part of the present refined plate theory. It is inspired by the general class of polynomial functions used in higher-order shear deformation theories, but its specific formulation—including the exponent n and the normalization term—was developed to ensure variational consistency and to satisfy the zero transverse shear stress conditions at the top and bottom surfaces of the plate. Unlike classical trigonometric warping functions such as those proposed by Reddy (1984) or Touratier (1991), which are fixed in shape, the proposed function introduces the parameter n, allowing for adjustable curvature across the thickness. This tunability enables the theory to adapt to different material gradations and loading conditions, especially in functionally graded and multilayered nanocomposite plates. The proposed formulation thus generalizes existing models and offers improved flexibility and accuracy while preserving analytical tractability.

2.3 Kinematic, strain and stress relations

Based on the assumptions outlined in the previous

section, the displacement field of the *n*-order four-variable refined theory is expressed as follows:

$$u(x,y,z) = u_0(x,y) - z\frac{\partial w_b}{\partial x} - \frac{z^r}{r}\left(\frac{2}{h}\right)^{r-1}\frac{\partial w_s}{\partial x} \tag{16}$$

$$v(x,y,z) = v_0(x,y) - z\frac{\partial w_b}{\partial y} - \frac{z^r}{r}\left(\frac{2}{h}\right)^{r-1}\frac{\partial w_s}{\partial y} \tag{17}$$

$$w(x,y,z) = w_b(x,y) + w_s(x,y) \tag{18}$$

The nonzero strains relating to the displacement field are:

$$\begin{Bmatrix}\varepsilon_x\\ \varepsilon_y\\ \gamma_{xy}\end{Bmatrix} = \begin{Bmatrix}\varepsilon_x^0\\ \varepsilon_y^0\\ \gamma_{xy}^0\end{Bmatrix} + z\begin{Bmatrix}k_x^b\\ k_y^b\\ k_{xy}^b\end{Bmatrix} + f(z)\begin{Bmatrix}k_s^s\\ k_s^s\\ k_{xy}^s\end{Bmatrix} \tag{19}$$

$$\begin{Bmatrix}\gamma_{xz}\\ \gamma_{yz}\end{Bmatrix} = g(z)\begin{Bmatrix}\gamma_{xz}^s\\ \gamma_{yz}^s\end{Bmatrix} \tag{20}$$

where

$$\begin{Bmatrix}\varepsilon_x^0\\ \varepsilon_y^0\\ \gamma_{xy}^0\end{Bmatrix} = \begin{Bmatrix}\dfrac{\partial u_0}{\partial x}\\ \dfrac{\partial v_0}{\partial y}\\ \dfrac{\partial u_0}{\partial y} + \dfrac{\partial v_0}{\partial x}\end{Bmatrix} \tag{21}$$

$$\begin{Bmatrix}k_x^b\\ k_y^b\\ k_{xy}^b\end{Bmatrix} = \begin{Bmatrix}-\dfrac{\partial^2 w_b}{\partial x^2}\\ -\dfrac{\partial^2 w_b}{\partial y^2}\\ -2\dfrac{\partial^2 w_b}{\partial x\partial y}\end{Bmatrix}, \qquad \begin{Bmatrix}k_x^s\\ k_y^s\\ k_{xy}^s\end{Bmatrix} = \begin{Bmatrix}-\dfrac{\partial^2 w_s}{\partial x^2}\\ -\dfrac{\partial^2 w_s}{\partial y^2}\\ -2\dfrac{\partial^2 w_s}{\partial x\partial y}\end{Bmatrix} \tag{22}$$

$$\begin{Bmatrix}\gamma_{xz}^s\\ \gamma_{yz}^s\end{Bmatrix} = \begin{Bmatrix}\dfrac{\partial w_s}{\partial x}\\ \dfrac{\partial w_s}{\partial y}\end{Bmatrix} \tag{23}$$

$$g(z) = 1 - \frac{df(z)}{dz} \tag{24}$$

The stress-strain relations for the *k*th-layer are expressed as (Arefi and Zenkour 2016):

$$\begin{Bmatrix}\sigma_x\\ \sigma_y\\ \tau_{yz}\\ \tau_{xz}\\ \tau_{xy}\end{Bmatrix}^{(k)} = \begin{bmatrix}Q_{11}^{(k)} & Q_{12}^{(k)} & 0 & 0 & 0\\ Q_{21}^{(k)} & Q_{22}^{(k)} & 0 & 0 & 0\\ 0 & 0 & Q_{44}^{(k)} & 0 & 0\\ 0 & 0 & 0 & Q_{55}^{(k)} & 0\\ 0 & 0 & 0 & 0 & Q_{66}^{(k)}\end{bmatrix}\begin{Bmatrix}\varepsilon_x\\ \varepsilon_y\\ \gamma_{yz}\\ \gamma_{xz}\\ \gamma_{xy}\end{Bmatrix}^{(k)} \tag{25}$$

where Q_{ij} represents the stiffness coefficients in terms of Young's modulus and Poisson's ratio, defined as

$$Q_{11}^{(k)} = Q_{22}^{(k)} = \frac{E_c^{(k)}}{1-\left(\nu_c^{(k)}\right)^2} \tag{26}$$

$$Q_{12}^{(k)} = Q_{21}^{(k)} = \frac{\nu_c^{(k)}E_c^{(k)}}{1-\left(\nu_c^{(k)}\right)^2} \tag{27}$$

$$Q_{44}^{(k)} = Q_{55}^{(k)} = Q_{66}^{(k)} = \frac{E_c^{(k)}}{2\left(1+\nu_c^{(k)}\right)} \tag{28}$$

Using Hamilton's principle, the governing differential equations are derived in terms of stress resultants and moment resultants, as follows:

$$\begin{aligned}
&\delta u_0\colon \frac{\partial N_x}{\partial x} + \frac{\partial N_{xy}}{\partial y} = 0\\
&\delta v_0\colon \frac{\partial N_{xy}}{\partial x} + \frac{\partial N_y}{\partial y} = 0\\
&\delta w_b\colon \frac{\partial^2 M_x^b}{\partial x^2} + 2\frac{\partial^2 M_{xy}^b}{\partial x\partial y} + \frac{\partial^2 M_y^b}{\partial y^2} + q + \overline{N} = 0\\
&\delta w_s\colon \frac{\partial^2 M_x^b}{\partial x^2} + 2\frac{\partial^2 M_{xy}^b}{\partial x\partial y} + \frac{\partial^2 M_y^b}{\partial y^2} + \frac{\partial S_{xz}^z}{\partial x} + \frac{\partial S_{yz}^z}{\partial y} + q + \overline{N} = 0
\end{aligned} \tag{29}$$

After performing mathematical operations and simplification, the equilibrium equations are rewritten in terms of displacements (u_0, v_0, w_b, w_s) as follows:

$$\begin{aligned}
&A_{11}\frac{\partial^2 u_0}{\partial x^2} + A_{66}\frac{\partial^2 u_0}{\partial y^2} + (A_{12}+A_{66})\frac{\partial^2 v_0}{\partial x\partial y}\\
&-B_{11}\frac{\partial^3 w_b}{\partial x^3} - (B_{12}+2B_{66})\frac{\partial^3 w_b}{\partial x\partial y^2} - B_{11}^s\frac{\partial^3 w_s}{\partial x^3}\\
&-(B_{12}^s+2B_{66}^s)\frac{\partial^3 w_s}{\partial x\partial y^2} = 0
\end{aligned} \tag{30a}$$

$$\begin{aligned}
&(A_{12}+A_{66})\frac{\partial^2 u_0}{\partial x\partial y} + A_{66}\frac{\partial^2 v_0}{\partial x^2} + A_{22}\frac{\partial^2 v_0}{\partial y^2}\\
&-(B_{12}+2B_{66})\frac{\partial^3 w_b}{\partial x^2\partial y} - B_{22}\frac{\partial^3 w_b}{\partial y^3}\\
&-B_{22}^s\frac{\partial^3 w_s}{\partial y^3} - (B_{12}^s+2B_{66}^s)\frac{\partial^3 w_s}{\partial x^2\partial y} = 0
\end{aligned} \tag{30b}$$

$$\begin{aligned}
&B_{11}\frac{\partial^3 u_0}{\partial x^3} + (B_{12}+2B_{66})\frac{\partial^3 u_0}{\partial x\partial y^2}\\
&+(B_{12}+2B_{66})\frac{\partial^3 v_0}{\partial x^2\partial y} + B_{22}\frac{\partial^3 v_0}{\partial y^3} - D_{11}\frac{\partial^4 w_b}{\partial x^4}\\
&-2(D_{12}+2D_{66})\frac{\partial^4 w_b}{\partial x^2\partial y^2} - D_{22}\frac{\partial^4 w_b}{\partial y^4} - D_{11}^s\frac{\partial^4 w_s}{\partial x^4}\\
&-2(D_{12}^s+2D_{66}^s)\frac{\partial^4 w_s}{\partial x^2\partial y^2} - D_{22}^s\frac{\partial^4 w_s}{\partial y^4} + q + \overline{N} = 0
\end{aligned} \tag{30c}$$

$$\begin{aligned}
&B_{11}^s\frac{\partial^3 u_0}{\partial x^3} + (B_{12}^s+2B_{66}^s)\frac{\partial^3 u_0}{\partial x\partial y^2}\\
&+(B_{12}^s+2B_{66}^s)\frac{\partial^3 v_0}{\partial x^2\partial y} + B_{22}^s\frac{\partial^3 v_0}{\partial y^3} - D_{11}^s\frac{\partial^4 w_b}{\partial x^4}\\
&-2(D_{12}^s+2D_{66}^s)\frac{\partial^4 w_b}{\partial x^2\partial y^2} - D_{22}^s\frac{\partial^4 w_b}{\partial y^4} - H_{11}^s\frac{\partial^4 w_s}{\partial x^4}\\
&-2(H_{12}^s+2H_{66}^s)\frac{\partial^4 w_s}{\partial x^2\partial y^2} - H_{22}^s\frac{\partial^4 w_s}{\partial y^4}
\end{aligned} \tag{30d}$$

$$+A_{55}^{s}\frac{\partial^2 w_s}{\partial x^2}+A_{44}^{s}\frac{\partial^2 w_s}{\partial y^2}+q+\overline{N}=0$$

where A_{ij}, B_{ij}, etc., are the plate stiffness coefficients, defined by

$$\{A_{ij},B_{ij},D_{ij},B_{ij}^{s},D_{ij}^{s},H_{ij}^{s}\}=\sum_{k=1}^{N_L}\int_{z_{(k)}}^{z_{(k+1)}}Q_{ij}^{(k)}\{1,z,z^2,f(z),zf(z),f^2(z)\}dz \quad (31a)$$

$$A_{44}^{s}=A_{55}^{s}=\sum_{k=1}^{N_L}\int_{z_{(k)}}^{z_{(k+1)}}Q_{44}^{(k)}[g(z)]^2dz \quad (31b)$$

3. Solution to the Problem

An analytical solution to the governing differential equations is obtained using the Navier solution technique for the nanocomposite plate, which is simply supported on all edges. The dimensionless displacement functions, satisfying the specified boundary conditions, are expressed as:

$$\begin{Bmatrix}u_0\\v_0\\w_b\\w_s\end{Bmatrix}=\sum_{m=1}^{M}\sum_{n=1}^{N}\begin{Bmatrix}U_{mn}\,cos(\lambda x)\,sin(\mu y)\\V_{mn}\,sin(\lambda x)\,cos(\mu y)\\W_{bmn}\,sin(\lambda x)\,sin(\mu y)\\W_{smn}\,sin(\lambda x)\,sin(\mu y)\end{Bmatrix} \quad (32)$$

where U_{mn}, V_{mn}, W_{bmn}, and W_{smn} are arbitrary parameters to be determined. Here, m and n represent the number of half-waves in the X- and Y-directions, respectively. The parameters λ and μ are defined as $\lambda = r\cdot\pi/a$ and $\mu = s\cdot\pi/b$. The transverse uniformly distributed load q is expanded using a double-Fourier sine series as:

$$q(x,y)=\sum_{m=1}^{\infty}\sum_{n=1}^{\infty}Q_{mn}\,sin(\lambda x)\,sin(\mu y) \quad (33)$$

The in-plane compressive load $\overline{N}$ is defined as:

$$\overline{N}=N_x^0\frac{\partial^2(w_b+w_s)}{\partial x^2}+N_y^0\frac{\partial^2(w_b+w_s)}{\partial y^2}+2N_{xy}^0\frac{\partial^2(w_b+w_s)}{\partial x\partial y} \quad (34)$$

By substituting Eqs. (32)-(34) into Eq. (30), the analytical solutions can be derived as:

$$\begin{bmatrix}S_{11}&S_{12}&S_{13}&S_{14}\\S_{12}&S_{22}&S_{23}&S_{24}\\S_{13}&S_{23}&S_{33}+k&S_{34}+k\\S_{14}&S_{24}&S_{34}+k&S_{44}+k\end{bmatrix}\begin{Bmatrix}U_{mn}\\V_{mn}\\W_{bmn}\\W_{smn}\end{Bmatrix}=\begin{Bmatrix}0\\0\\Q_{mn}\\Q_{mn}\end{Bmatrix} \quad (35)$$

in which

$$\begin{aligned}
S_{11}&=A_{11}\lambda^2+A_{66}\mu^2\\
S_{12}&=\lambda\mu(A_{12}+A_{66})\\
S_{13}&=-\lambda(B_{11}\lambda^2+(B_{12}+2B_{66})\mu^2)\\
S_{14}&=-\lambda(B_{11}^{s}\lambda^2+(B_{12}^{s}+2B_{66}^{s})\mu^2)\\
S_{22}&=A_{66}\lambda^2+A_{22}\mu^2\\
S_{23}&=-\mu\big((B_{12}+2B_{66})\lambda^2+B_{22}\mu^2\big)\\
S_{24}&=-\mu\big((B_{12}^{s}+2B_{66}^{s})\lambda^2+B_{22}^{s}\mu^2\big)
\end{aligned} \quad (36)$$

$$\begin{aligned}
S_{33}&=D_{11}\lambda^4+2(D_{12}+2D_{66})\lambda^2\mu^2+D_{22}\mu^4\\
S_{34}&=D_{11}^{s}\lambda^4+2(D_{12}^{s}+2D_{66}^{s})\lambda^2\mu^2+D_{22}^{s}\mu^4\\
S_{44}&=H_{11}^{s}\lambda^4+2(H_{12}^{s}+2H_{66}^{s})\lambda^2\mu^2+H_{22}^{s}\mu^4\\
&+A_{55}^{s}\lambda^2+A_{44}^{s}\mu^2(36)
\end{aligned}$$

$$k=-N_0(\lambda^2+\gamma\mu^2) \quad (37)$$

Assuming that the multilayer GPL/polymer nanocomposite plate is subjected to in-plane compressive loads $N_x^0=-N_0$, $N_y^0=-\gamma N_0$, and $N_{xy}^0=0$. Here γ is non-dimensional load parameter. For bi-axial compressive load, it is $\gamma = 1$

4. Numerical results and discussion

This section provides an extensive parametric analysis of the bending and buckling behavior of functionally graded multilayer GPL/polymer plates, with a focus on the influence of GPL nanofiller distribution patterns and weight fractions. The numerical results are systematically arranged and presented in tables for clarity.

4.1 Static bending

As an illustrative example, a uniformly distributed load $q(x, y)$ is considered, where in Eq. (33) we have:

$$q_{mn}=\frac{16q_0}{mn\pi^2} \quad (38)$$

Since no existing literature provides results for the bending response of graphene-based nanocomposite plates, a simply supported aluminum/alumina (Al/ZrO_2) functionally graded square plate is analyzed to validate the current bending analysis. The material properties are as follows:

- Aluminum (Al): E_1 = 70 GPa, ν_1 = 0.3
- Zirconia (ZrO_2): E_2 = 200 GPa, ν_2 = 0.3

It is assumed that the top and bottom surfaces of the plate are ZrO_2-rich and Al-rich, respectively. The effective material properties, $P(z)$, are graded through the thickness according to a power law based on the volume fractions of the constituent materials:

$$P(z)=P_2+(P_1-P_2)\cdot V(z) \quad (39)$$

where $V(z)$ is defined as:

$$V(z)=\left(\frac{z}{h}+\frac{1}{2}\right)^{p},\quad p\geq 0 \quad (40)$$

Here, P_1 and P_2 represent the material properties of ZrO_2 and Al, respectively, while p denotes the volume fraction index. Using the equivalent homogeneous laminated structure approach, the functionally graded plate is divided into a finite number of isotropic and homogeneous layers through the thickness direction. The equivalent effective material property of each layer is computed as the average value of Eq. (38) within the layer:

$$P_{eq}^{(k)}=\int_{z_k}^{z_{k+1}}\frac{P(z)}{Z_{k+1}-Z_k}dz,\quad k=1,2,\dots,N_L \quad (41)$$

To ensure accuracy, a convergence study is performed

Table 1 Dimensionless central displacement w_c of a square Al/ZrO_2 functionally graded plate under uniform load (p=0.5)

N_L	Theory		M=1, N=1	M=10, N=10	M=20, N=20
10	Song *et al*. (2018)		0.2408	0.2319	0.2318
	Present	n = 3	0.2402	0.2312	0.2312
		n = 5	0.2395	0.2306	0.2306
		n = 7	0.2386	0.2297	0.2297
20	Song *et al*. (2018)		0.2413	0.2323	0.2323
	Present	n = 3	0.2407	0.2317	0.2317
		n = 5	0.2399	0.2311	0.2311
		n = 7	0.2390	0.2302	0.2302
30	Song *et al*. (2018)		0.2414	0.2324	0.2324
	Present	n = 3	0.2368	0.2284	0.2284
		n = 5	0.2362	0.2279	0.2279
		n = 7	0.2354	0.2272	0.2272

Table 2 Comparison of dimensionless central displacement of a square Al/ZrO_2 functionally graded plate under uniform load (a/h=5, N_L = 10, M = N = 10)

Theory		p			
		0	0.5	1	2
Song *et al*. (2018)		0.1717	0.2319	0.2716	0.3121
Nguyen-Xuan *et al*. (2011)		0.1703	0.2232	0.2522	0.2827
Gilhooley *et al*. (2007)		0.1671	0.2505	0.2905	0.3280
Lee *et al*. (2009)		0.1722	0.2403	0.2811	0.3221
Present	n = 3	0.1716	0.2312	0.2715	0.3139
	n = 5	0.1710	0.2306	0.2706	0.3124
	n = 7	0.1703	0.2298	0.2696	0.3108

and summarized in Table 1. The dimensionless central displacement w_c is expressed as:

$$w_c = \frac{100 W_c E_1 h^3}{12(1-\nu^2) q_0 a^4} \tag{42}$$

The study compares the results for a functionally graded plate with varying truncated series terms M, N and the total number of layers N_L. It is observed that convergence is achieved when M = N = 10 for the double series solution (Eq. 32) and N_L = 10.

The study compares the results for a functionally graded plate with varying truncated series terms M, N and the total number of layers N_L. It is observed that convergence is achieved when M = N = 10 for the double series solution (Eq. 32) and N_L = 10.

The results presented in Table 2 demonstrate the dimensionless central displacement of a square Al/ZrO_2 functionally graded plate under uniform loading conditions. The comparison is made across multiple theories, including the first-order shear deformation plate theory (Song *et al*. 2018), the edge-based smoothed finite element method (Nguyen-Xuan *et al*. 2011), the meshless local Petrov-Galerkin (MLPG) method (Gilhooley *et al*. 2007), and the element-free kp-Ritz method (Lee *et al*. 2009). The table shows excellent agreement between the present method and existing results, validating the accuracy of the proposed n-order refined plate theory.

For various values of the material gradation parameter p, the results from the present study for n=3, 5, and 7 align closely with those from previous methods. As p increases, indicating a higher gradation of material properties, all approaches predict increasing central displacement, reflecting the impact of material heterogeneity on structural behavior. Notably, the present method slightly underestimates the displacement for higher values of p compared to methods such as the MLPG and kp-Ritz, but the differences remain minimal, demonstrating the robustness of the proposed approach. These findings confirm the effectiveness of the present refined theory in accurately capturing the bending response of functionally graded plates.

In the following analysis, graphene nanoplatelet (GPL)-reinforced polymer composite plates of dimensions 0.45 m×0.45 m×0.045 m are considered. Epoxy was chosen as the matrix material due to its excellent mechanical properties, low density, and strong adhesion to reinforcement materials, making it ideal for lightweight composite structures. Additionally, epoxy exhibits high thermal and chemical stability, ensuring durability in various engineering applications. Its ability to effectively disperse GPLs further enhances the mechanical performance of the nanocomposite, making it a preferred choice for achieving improved stiffness and strength in GPL-reinforced polymer composites. The material properties are given as:

- Epoxy: ρ_M = 1.2 g/cm^3, E_M = 3.0 GPa, v_M = 0.34
- GPL: ρ_{GPL} = 1.01 TPa, E_{GPL}= 1.01 TPa, v_{GPL} = 0.186

The total number of layers N_L is assumed to be an even number, and the GPL weight fraction in the k-th layer for four distinct GPL distribution patterns is defined as:

$$g_{GNP}^{(k)} = \begin{cases} g_{GPL}^{*} & \text{for UD} \\ \dfrac{4 g_{GPL}^{*}\left(\frac{N_L+1}{2} - \left|k - \frac{N_L+1}{2}\right|\right)}{2+N_L} & \text{for FG-O} \\ \dfrac{4 g_{GPL}^{*}\left(\frac{1}{2} + \left|k - \frac{N_L+1}{2}\right|\right)}{2+N_L} & \text{for FG-X} \\ \dfrac{4k g_{GPL}^{*}}{(N_L+1)} & \text{for FG-A} \end{cases} \tag{43}$$

Here, g^*_{GPL} represents the total weight fraction of graphene nanoplatelets, and k=1, 2, … , N_L. Unless otherwise stated, the GPL dimensions are l_{GPL} = 2.5 μm, w_{GPL} = 1.5 μm, and h_{GPL} = 1.5 μm, with a total weight fraction of 1.0%. The uniformly distributed load q_0 is taken as 500 kPa.

Fig. 3 illustrates the effect of the GPL weight fraction g^*_{GPL} on the deflection ratio W_C/W_M for GPL/epoxy nanocomposite plates under different distribution patterns. The results indicate a significant reduction in central deflection as the GPL weight fraction increases for all distribution patterns.

Additionally, the GPL distribution pattern plays a critical role in the static deflection behavior of the plate. For

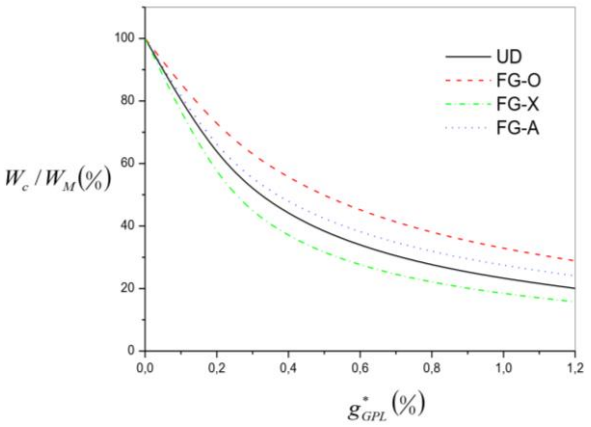

Fig. 3 Effect of GPL weight fraction on W_C/W_M of functionally graded multilayer GPL/epoxy

Table 3 Comparison of nondimensional critical buckling load of simply supported isotropic square plates subjected to uniaxial and biaxial compressive loads.

Load type	Theories		a/h = 5	10	20	50
Uniaxial compression	Song *et al*. (2018)		2.9498	3.4222	3.5648	3.6000
	Sayyad and Ghugal (2014)		3.0266	3.4541	3.5821	3.6013
	Reddy (1984)		2.9512	3.4224	3.5649	3.6068
	Present	n = 3	2.9512	3.4224	3.5649	3.6071
		n = 5	2.9614	3.4260	3.5659	3.6073
		n = 7	2.9745	3.4304	3.5672	3.6075
Biaxial compression	Song *et al*. (2018)		1.4749	1.7111	1.7824	1.8000
	Sayyad and Ghugal (2014)		1.5133	1.7271	1.7910	1.8106
	Reddy (1984)		1.4756	1.7112	1.7825	1.8034
	Present	n = 3	1.4756	1.7112	1.7825	1.8036
		n = 5	1.4807	1.7130	1.7130	1.8036
		n = 7	1.4872	1.7152	1.7836	1.8037

the same GPL weight fraction, the FG-X distribution pattern yields the smallest deflection, followed by UD, FG-A, and then FG-O. The FG-X distribution pattern results in the smallest deflection among the considered configurations because it strategically places a higher concentration of GPLs near the top and bottom surfaces of the composite plate. In bending scenarios, these regions experience the largest normal stresses due to their distance from the neutral axis. By increasing the reinforcement in these critical areas, the FG-X distribution maximizes the stiffness and load-carrying capacity of the plate, effectively reducing its deflection.

In contrast, other patterns such as FG-O and FG-A distribute GPLs in ways that are less aligned with the stress distribution under bending. The FG-O pattern concentrates GPLs at the mid-plane, where normal stresses are minimal, resulting in a less effective reinforcement strategy and higher deflection. FG-A introduces an asymmetric GPL distribution, which does not match the symmetric nature of bending-induced stresses in simply supported plates under uniform loading. Although FG-A performs slightly better than FG-O, it still underperforms compared to the FG-X configuration. The superior performance of FG-X is attributed to its strategic placement of GPLs near the top and bottom surfaces, where the bending stresses are highest, thereby maximizing stiffness and minimizing deflection.

The weight fraction of GPLs significantly impacts the stiffness of the composite plate. Higher weight fractions introduce more GPLs into the polymer matrix, enhancing load transfer and increasing resistance to bending deformations due to GPLs' superior mechanical properties. This effect is most pronounced when GPLs are optimally distributed, such as in FG-X patterns, where they reinforce high-stress regions. However, excessively high weight fractions may lead to filler agglomeration, limiting further stiffness improvements. Balancing weight fraction and distribution is crucial for maximizing composite performance.

4.2 Elastic buckling

The bending-stretching coupling effect is a well-documented phenomenon in laminated composite plates, where even small in-plane forces can induce significant deflections and bending moments, particularly in plates with asymmetric lamination (Leissa 1986). Consequently, bifurcation-type compressive buckling cannot occur in simply supported FG-A plates, as their unsymmetrical GPL distribution leads to inherent bending-stretching coupling. Therefore, the elastic buckling analysis in this section is focused exclusively on UD, FG-O, and FG-X plates, which feature symmetrical GPL distributions. These configurations allow for a more direct assessment of the buckling behavior without the complications introduced by asymmetric material properties.

A simply supported isotropic square plate (E = 210 GPa, ν = 0.3) subjected to a uniaxial compression along the X-direction (γ = 0) and equal biaxial compression (γ = 1) is considered. Table 3 provides a comparison of nondimensional critical buckling loads $\left(\overline{N}_{cr} = N_{cr}a^2/Eh^3\right)$ for a simply supported isotropic square plate under uniaxial and biaxial compressive loads, considering various a/h ratios. The critical buckling loads obtained using the present method are compared with those from established studies by Song *et al*. (2018), Sayyad and Ghugal (2014) and Reddy (1984). The results demonstrate excellent agreement across all a/h ratios, validating the accuracy and robustness of the proposed method.

Under uniaxial compression, the present method closely matches the results from the referenced theories, with minor variations as the parameter n increases. The critical buckling loads slightly increase with larger n values, indicating that the proposed refined plate theory captures additional stiffness contributions effectively. The trends align consistently with the benchmark studies, show casingthe reliability of the present approach.

For biaxial compression, the critical buckling loads are similarly well-predicted by the present method, showing strong concordance with the referenced theories. The results

Table 4 Dimensionless critical buckling loads of functionally graded multilayer GPL/epoxy plates under uniaxial and equal biaxial compressions (n=3), for pure epoxy and g^*_{GPL} values 0.2%, 0.4%

			g^*_{GPL}	
		Pure Epoxy	0.2%	0.4%
Uniaxial compression (γ = 0)				
Present	UD	0.0035	0.0058	0.00817
Song *et al*. (2018)		0.0035	0.0058	0.0082
Present	FG-O	0.0035	0.00497	0.00642
Song *et al*. (2018)		0.0035	0.0050	0.0064
Present	FG-X	0.0035	0.00667	0.00980
Song *et al*. (2018)		0.0035	0.0067	0.0099
Biaxial compression (γ = 1)				
Present	UD	0.00175	0.00292	0.0040
Song *et al*. (2018)		0.0018	0.0029	0.0041
Present	FG-O	0.00175	0.00248	0.0032
Song *et al*. (2018)		0.0018	0.0025	0.0032
Present	FG-X	0.00175	0.00333	0.00490
Song *et al*. (2018)		0.0018	0.0034	0.0050

Table 5 Dimensionless critical buckling loads of functionally graded multilayer GPL/epoxy plates under uniaxial and equal biaxial compressions (n=3), for g^*_{GPL} values 0.2%, 0.4% and 0.6%

		g^*_{GPL}		
		0.6%	0.8%	1.0%
Uniaxial compression (γ = 0)				
Present	UD	0.00105	0.01284	0.01517
Song *et al*. (2018)		0.0105	0.0128	0.0152
Present	FG-O	0.00786	0.00931	0.01075
Song *et al*. (2018)		0.0078	0.0093	0.0107
Present	FG-X	0.01292	0.01604	0.01915
Song *et al*. (2018)		0.0131	0.0163	0.0195
Biaxial compression (γ = 1)				
Present	UD	0.00525	0.00642	0.00758
Song *et al*. (2018)		0.0053	0.0064	0.0076
Present	FG-O	0.00393	0.00465	0.00537
Song *et al*. (2018)		0.0039	0.0046	0.0053
Present	FG-X	0.00646	0.00802	0.00957
Song *et al*. (2018)		0.0066	0.0082	0.0097

highlight that the proposed method provides slightly higher critical loads for larger n values compared to other methods, particularly for higher a/h ratios. This suggests that the proposed method is capable of accurately modeling the enhanced stability effects associated with biaxial loading conditions.

Overall, the data in Table 3 confirm the capability of the proposed n-order refined plate theory to accurately predict the critical buckling loads and bending responses of isotropic and functionally graded nanocomposite plates under both uniaxial and biaxial compressive loads. The strong agreement with established methods—such as the first-order shear deformation theory (FSDT), the MLPG method, and the element-free kp-Ritz method—reinforces the validity of the analytical framework and also highlights its accuracy and reliability. These benchmark comparisons confirm that the proposed theory effectively captures the essential mechanical behavior of advanced composite structures without the need for shear correction factors, demonstrating its robustness and suitability for a wide range of structural applications.

The impact of the GPL weight fraction (g^*_{GPL}) on the dimensionless critical buckling loads for UD, FG-O, and FG-X plates under uniaxial (γ=0) and equal biaxial (γ=1) compressions is presented in Table 4 and Table 5. Table 4 also includes results for a pure epoxy plate to provide a baseline for comparison. These results highlight the significant reinforcing effect of GPL nanofillers on the critical buckling loads of the composite plates, even at low concentrations.

The comparison reveals that GPL-reinforced plates exhibit much higher critical buckling loads than pure epoxy plates, underscoring the remarkable mechanical benefits of incorporating GPL nanofillers. For all configurations, the critical buckling load increases substantially with the GPL weight fraction. Among the three distribution patterns, FG-X demonstrates the highest critical buckling loads, followed by UD and FG-O, regardless of the loading condition. This indicates that the FG-X distribution, which places higher concentrations of GPLs near the outer surfaces of the plate, is the most effective in enhancing stiffness and buckling resistance. Conversely, the FG-O pattern, which concentrates GPLs near the mid-plane, shows the lowest buckling loads due to less effective reinforcement in regions of high stress.

Under uniaxial compression (γ=0), the critical buckling loads of all GPL-reinforced configurations consistently increase with g^*_{GPL}. For instance, in the FG-X configuration, the critical load rises from 0.0035 for pure epoxy to 0.01915 at 1.0% weight fraction. This highlights the substantial improvement in stability achieved by optimizing GPL distribution and concentration. The UD configuration shows a similar trend, albeit with slightly lower critical loads compared to FG-X, reflecting its uniform reinforcement distribution.

For equal biaxial compression (γ=1), the trends are consistent with those observed for uniaxial loading, but the critical buckling loads are slightly lower across all configurations. This reflects the inherent challenges of resisting buckling under biaxial stresses, where the load is distributed more evenly across the plate. Nevertheless, the FG-X configuration still outperforms UD and FG-O, achieving the highest critical loads at all GPL weight fractions.

In summary, the results in Table 4 and Table 5 confirm that the inclusion of GPLs significantly enhances the buckling performance of polymer composite plates, with FG-X being the optimal distribution for maximizing critical

buckling loads. These findings demonstrate the importance of strategically distributing GPLs within the composite to align with stress regions, thereby achieving superior mechanical performance. Additionally, the slightly better reinforcement effect under uniaxial compression compared to biaxial compression emphasizes the need to consider loading conditions in the design of GPL-reinforced structures.

5. Conclusions

This study presented a comprehensive investigation of the bending and buckling behaviors of functionally graded multilayer GPL/polymer nanocomposite plates using a novel n-order refined plate theory. The theory employed higher-order polynomial displacement fields, ensuring variational consistency and eliminating the need for shear correction factors. Analytical solutions for static deflection and buckling were derived using the Navier solution technique, providing accurate results consistent with boundary conditions.

Through a detailed parametric study, this work identified the critical influence of key parameters on the mechanical performance of the plates:

• Non-uniform distribution patterns (FG-O, FG-X, FG-A) exhibited distinct bending and buckling responses compared to the uniform distribution (UD). Among these, FG-X demonstrated superior performance by strategically reinforcing regions of higher stress, while FG-O and FG-A displayed less effective reinforcement due to their respective GPL arrangements. This highlights the importance of tailored GPL distributions to optimize structural performance.

• Increasing the GPL weight fraction resulted in significant improvements in stiffness, reductions in deflection, and enhancements in buckling resistance. This emphasizes the critical role of filler concentration in achieving optimal mechanical behavior for nanocomposite plates.

• Optimizing the aspect ratios and increasing the surface area of GPLs significantly enhanced reinforcement efficiency, improving the plates' ability to withstand higher loads and resist deformation.

• The study revealed that the reinforcing effect of GPL nanofillers is more pronounced under uniaxial compression compared to equal biaxial compression, demonstrating the need to consider loading scenarios when designing functionally graded nanocomposite plates.

The insights gained from this study provide valuable guidance for the design and optimization of lightweight, high-performance GPL-reinforced polymer nanocomposites. These materials hold immense potential for applications across various industries. In aerospace, they can be used to develop lightweight yet strong components for improving fuel efficiency. In the automotive sector, they offer structural integrity while reducing weight, and in civil engineering, they provide advanced construction materials with enhanced load-bearing capacities.

Among the various GPL distribution patterns studied, the FG-X configuration is especially well-suited for such applications, as it places reinforcements near the surfaces where bending stresses are highest. This makes it particularly advantageous in aerospace components (e.g., wing skins, fuselage panels), automotive structures (e.g., body panels, battery enclosures), and civil infrastructure (e.g., slabs, bridge decks), where maximizing stiffness and buckling resistance while minimizing weight is critical.

This research establishes a foundation for further studies on GPL-reinforced polymer nanocomposites. Future work could explore thermal effects on bending and buckling behavior, dynamic loading conditions such as vibrations and impacts, and experimental validation to align theoretical predictions with real-world performance. Additionally, combining GPLs with other nanofillers may create hybrid composites with enhanced properties. Advancements in 3D printing could enable precise control over material distribution and geometry, unlocking new possibilities for designing and applying functionally graded nanocomposite structures in engineering and industrial contexts.

References

Ansari, R. and Norouzzadeh, A. (2016), "Nonlocal and surface effects on the buckling behavior of functionally graded nanoplates: An isogeometric analysis", *Physica E*, **84**, 84-97. https://doi.org/10.1016/j.physe.2016.05.036.

Ansari, R., Shakouri, A. H., Bazdid-Vahdati, M., Norouzzadeh, A. and Rouhi, H. (2017), "A nonclassical finite element approach for the nonlinear analysis of micropolar plates", *J. Comput. Nonlinear Dyn.*, **12**(1). https://doi.org/10.1115/1.4034678.

Ansari, R., Torabi, J. and Norouzzadeh, A. (2018), "Bending analysis of embedded nanoplates based on the integral formulation of Eringen's nonlocal theory using the finite element method", *Physica B*, **534**, 90-97 https://doi.org/10.1016/j.physb.2018.01.025.

Arefi, M. and Zenkour, A. M. (2016), "Employing sinusoidal shear deformation plate theory for transient analysis of three layers sandwich nanoplate integrated with piezo-magnetic face-sheets", *Smart Mater. Struct.*, **25**(11), 115040. https://doi.org/10.1088/0964-1726/25/11/115040.

Bellucci, S., Balasubramanian, C., Micciulla, F. and Rinaldi, G. (2007), "CNT composites for aerospace applications", *J. Experim. Nanosci.*, **2**(3), 193-206. https://doi.org/10.1080/17458080701376348.

Cong, P.H. and Duc, N.D. (2018), "New approach to investigate the nonlinear dynamic response and vibration of a functionally graded multilayer graphene nanocomposite plate on a viscoelastic Pasternak medium in a thermal environment", *Acta Mechanica*, **229**(9), 3651-3670. https://doi.org/10.1007/s00707-018-2178-3.

Daikh, A.A., Hamdi, A., Ahmed, H.M., Abdelwahed, M.S., Abdelrahman, A.A. and Eltaher, M.A. (2023), "Buckling and bending of coated FG graphene-reinforced composite plates and shells", *Adv. Nano Res.*, **15**(2), 113-128. https://doi.org/10.12989/anr.2023.15.2.113.

Drai, A., Daikh, A.A., Belarbi, M.O., Houari, M.S.A., Aour, B., Hamdi, A. and Eltaher, M.A. (2023), "Bending of axially functionally graded carbon nanotubes reinforced composite nanobeams", *Adv. Nano Res.*, **14**(3), 211-224. https://doi.org/10.12989/anr.2023.14.3.211.

Ebrahimi, F., Ezzati, H. and Najafi, M. (2024), "Wave propagation analysis of functionally graded nanocomposite plate reinforced with graphene platelets in presence of thermal excitation", *Acta*

Mechanica, **235**(1), 215-234. https://doi.org/10.1007/s00707-023-03728-7.

Gilhooley, D.F., Batra, R.C., Xiao, J.R., McCarthy, M.A. and Gillespie, J.W. (2007), "Analysis of thick functionally graded plates by using higher-order shear and normal deformable plate theory and MLPG method with radial basis functions", *Compos. Struct.*, **80**(4), 539-552. https://doi.org/10.1016/j.compstruct.2006.07.007.

Huang, X., Qi, X., Boey, F. and Zhang, H. (2012), "Graphene-based composites", *Chem. Soc. Rev.*, **41**(2), 666-686. https://doi.org/10.1039/C1CS15078B.

Joueid, N., Zghal, S., Chrigui, M. and Dammak, F. (2024), "Thermoelastic buckling analysis of plates and shells of temperature and porosity dependent functionally graded materials", *Mech. Time Depend. Mater.*, **28**(3), 817-859. https://doi.org/10.1007/s11043-023-09644-6.

Lee, Y.Y., Zhao, X. and Liew, K.M. (2009), "Thermoelastic analysis of functionally graded plates using the element-free kp-Ritz method", *Smart Mater. Struct.*, **18**(3), 035007. https://doi.org/10.1088/0964-1726/18/3/035007.

Leissa, A.W. (1986), "Conditions for laminated plates to remain flat under inplane loading", *Compos. Struct.*, **6**(4), 261-270. https://doi.org/10.1016/0263-8223(86)90022-X.

Moita, J.S., Araújo, A.L., Correia, V.F., Mota Soares, C.M. and Herskovits, J. (2020), "Buckling behavior of composite and functionally graded material plates", *Eur. J. Mech. A Solids*, **80**, 103921. https://doi.org/10.1016/j.euromechsol.2019.103921.

Montazeri, A. and Rafii-Tabar, H. (2011), "Multiscale modeling of graphene- and nanotube-based reinforced polymer nano-composites", *Phys. Lett. A*, **375**(45), 4034-4040. https://doi.org/10.1016/j.physleta.2011.08.073.

Mortazavi, B., Benzerara, O., Meyer, H., Bardon, J. and Ahzi, S. (2013), "Combined molecular dynamics-finite element multiscale modeling of thermal conduction in graphene epoxy nanocomposites", *Carbon*, **60**, 356-365. https://doi.org/10.1016/j.carbon.2013.04.048.

Nguyen-Xuan, H., Tran, L.V., Nguyen-Thoi, T. and Vu-Do, H.C. (2011), "Analysis of functionally graded plates using an edge-based smoothed finite element method", *Compos. Struct.*, **93**(11), 3019-3039. https://doi.org/10.1016/j.compstruct.2011.04.028.

Norouzzadeh, A. and Ansari, R. (2018), "Isogeometric vibration analysis of functionally graded nanoplates with the consideration of nonlocal and surface effects", *Thin Wall. Struct.*, **127**, 354-372. https://doi.org/10.1016/j.tws.2017.11.040.

Norouzzadeh, A., Ansari, R. and Rouhi, H. (2018), "Isogeometric analysis of Mindlin nanoplates based on the integral formulation of nonlocal elasticity", *Multidiscipl. Model. Mater. Struct.*, **14**(5), 810-827. https://doi.org/10.1108/MMMS-09-2017-0109.

Potts, J.R., Dreyer, D.R., Bielawski, C.W. and Ruoff, R.S. (2011), "Graphene-based polymer nanocomposites", *Polymer*, **52**(1), 5-25. https://doi.org/10.1016/j.polymer.2010.11.042.

Rafiee, M.A., Rafiee, J., Srivastava, I., Wang, Z., Song, H., Yu, Z.Z. and Koratkar, N. (2010), "Fracture and fatigue in graphene nanocomposites", *Small*, **6**(2), 179-183. https://doi.org/10.1002/smll.200901480.

Rafiee, M.A., Rafiee, J., Wang, Z., Song, H., Yu, Z.Z. and Koratkar, N. (2009a), "Enhanced mechanical properties of nanocomposites at low graphene content", *ACS Nano*, **3**(12), 3884-3890. https://doi.org/10.1021/nn9010472.

Rafiee, M.A., Rafiee, J., Yu, Z.Z. and Koratkar, N. (2009b), "Buckling resistant graphene nanocomposites", *Appl. Phys. Lett.*, **95**(22), 223103. https://doi.org/10.1063/1.3269637.

Reddy, J.N. (1984), "A simple higher-order theory for laminated composite plates", *J. Appl. Mech.*, **51**(4), 745-752. https://doi.org/10.1115/1.3167719.

Sayyad, A.S. and Ghugal, Y.M. (2014), "On the buckling of isotropic, transversely isotropic and laminated composite rectangular plates", *Int. J. Struct. Stabil. Dyn.*, **14**(7), 1450020. https://doi.org/10.1142/S0219455414500205.

Sitli, Y., Mhada, K., Bourihane, O. and Rhanim, H. (2021), "Buckling and post-buckling analysis of a functionally graded material (FGM) plate by the Asymptotic Numerical Method", *Structures*, **31**, 1031-1040. https://doi.org/10.1016/j.istruc.2021.01.100.

Song, M., Kitipornchai, S. and Yang, J. (2017), "Free and forced vibrations of functionally graded polymer composite plates reinforced with graphene nanoplatelets", *Compos. Struct.*, **159**, 579-588. https://doi.org/10.1016/j.compstruct.2016.09.070.

Song, M., Yang, J. and Kitipornchai, S. (2018), "Bending and buckling analyses of functionally graded polymer composite plates reinforced with graphene nanoplatelets", *Compos. Part B Eng.*, **134**, 106-113. https://doi.org/10.1016/j.compositesb.2017.09.043.

Swaminathan, K., Sachin, H. and Rajanna, T. (2021), "Buckling analysis of functionally graded materials by dynamic approach", *Mater. Today Proc.*, **45**, 172-178. https://doi.org/10.1016/j.matpr.2020.10.412.

Touratier, M. (1991), "An efficient standard plate theory", *Int. J. Eng. Sci.*, **29**(8), 901-916. https://doi.org/10.1016/0020-7225(91)90165-Y.

Wang, Y., Yu, J., Dai, W., Song, Y., Wang, D., Zeng, L. and Jiang, N. (2015), "Enhanced thermal and electrical properties of epoxy composites reinforced with graphene nanoplatelets", *Polym. Compos.*, **36**(3), 556-565. https://doi.org/10.1002/pc.22972.

Xiang, S., Jin, Y.X., Bi, Z.Y., Jiang, S.X. and Yang, M.S. (2011), "A n-order shear deformation theory for free vibration of functionally graded and composite sandwich plates", *Compos. Struct.*, **93**(11), 2826-2832. https://doi.org/10.1016/j.compstruct.2011.05.022.

CC